

Geometrically manipulating photonic Schrödinger cat states and realizing two-logical-qubit gates

Y. Xu,^{1,*} Y. Ma,^{1,*} W. Cai,¹ X. Mu,¹ W. Dai,¹ W. Wang,¹ L. Hu,¹ X. Li,¹ J. Han,¹
H. Wang,¹ Y. P. Song,¹ Zhen-Biao Yang,^{2,†} Shi-Biao Zheng,^{2,‡} and L. Sun^{1,§}

¹*Center for Quantum Information, Institute for Interdisciplinary Information Sciences, Tsinghua University, Beijing 100084, China*

²*Fujian Key Laboratory of Quantum Information and Quantum Optics,*

College of Physics and Information Engineering, Fuzhou University, Fuzhou, Fujian 350108, China

Geometric phases are of particular importance for manipulation of quantum states and for quantum information processing. Here, we show that a transmon qubit can be forced to traverse a circuit, accumulating a geometric phase, conditional on the photon number of one or two cavities dispersively coupled to the qubit. Based on this geometric effect, we demonstrate the photon-number parity of a Schrödinger cat state in a cavity can be controlled, offering the possibility for correcting the parity flip due to single-photon loss. We further geometrically realize phase gates for one and two photonic qubits with logical basis states encoded in two quasiorthogonal coherent states, which have important implications for continuous-variable-based quantum computation. More importantly, we use this geometric method to implement a controlled-phase gate between two logical qubits binomially encoded in error-correctable logical space, which represents an important step towards fault-tolerant quantum computation.

When a quantum system is parallel-transported along a circuit in its quantum state space, it collects information about the geometry of this path, acquiring a “memory” of its motion in the form of a phase. This phase is referred to as the geometric phase and has close relations to many physical phenomena [1, 2]. This effect was first discovered by Berry in the context of adiabatic passage [3]. One remarkable feature of Berry phase is that it is robust against fast parameter fluctuations whose effect on the enclosed parameter-space area averages out [4]. As such, Berry phase has been considered as a choice for fault-tolerant quantum computation [5, 6]. So far, observation of this phase and demonstration of its noise-resilient feature have been reported in various physical systems [6–11]. Berry’s discovery has triggered considerable interest in quantum-mechanical geometric effects, leading to important generalizations in various directions [12, 13]. In particular, Aharonov and Anandan defined geometric phase in the projective Hilbert space, instead of in parameter space [12], removing the adiabatic condition. The geometric nature of Aharonov-Anandan (AA) phase lies in the fact that it is related to the area enclosed by the circuit traversed by the state vector.

When two or more quantum systems are coupled, the geometric phase acquired by one system can be employed to manipulate the quantum state of the others [10, 14]. The geometric phase of a harmonic vibrational mode of trapped ions has been utilized for implementing high-fidelity entangling gates for the ionic qubits [15]. In a recent experiment [16], the geometric phase of a continuous-variable field mode was observed through Ramsey interference and used for realizing controlled-phase gates with up to four qubits in a superconducting circuit. On the other hand, it has been shown that the geometric phase of a superconducting qubit can be used for realizing Selective Number-dependent Arbitrary Phase (SNAP) gates on a cavity [17]. This kind of gates has been experimentally demonstrated and used to produce a single-photon state [18]. Recently, a quantum controlled-NOT gate between two photonic qubits respectively stored in

two cavities has been demonstrated by use of both the dynamical and AA phases [19]. This gate was realized by encoding the codewords of the control qubit on the vacuum state and two-photon state, which form a logical space where errors due to photon loss cannot be corrected. Entangling gate operations between error-correctable logical qubits, required by fault-tolerant quantum computation, still remain elusive.

We here show that the geometric phase acquired by a transmon qubit can be used to manipulate a cat state in a cavity dispersively coupled to the qubit, and to realize controlled-phase gates for photonic qubits in two cavities with different encodings, in particular for two error-correctable logical qubits. Cat states are of fundamental interest [20] and can be used to encode logical qubits [21–24]. Thus, manipulating these states and protecting them from decoherence is a subject of great importance. In our experiment, the qubit is parallel-transported along a closed loop on the Bloch sphere, picking up a geometric phase, conditional on the particular component of the photonic qubits. We demonstrate the photon-number parity of the cat state can be manipulated by this geometric operation. This manipulation technique, in combination with the parity jump tracking method [25], allows for the correction of parity flip of cat states due to single-photon loss. We then employ this geometric phase to realize single- and two-cavity phase gates for the coherent-state-encoded qubits. We further extend our method to implement a controlled-Z (CZ) gate between two binomial logical qubits with inherent error correction function. The demonstrated entangling gate between error-correctable logical qubits represents an important step towards fault-tolerant quantum computation. The procedure can be straightforwardly and easily generalized to realize phase gates among multiple error-correctable logical qubits.

The experiments presented in this work are based on two circuit quantum electrodynamics (QED) devices [26–30]. Device A, on which single-cavity geometric phase gates are performed, consists of two transmon qubits simultaneously dispersively coupled to two three-dimensional cavities [31–35]. The parameters and architecture setup are described in

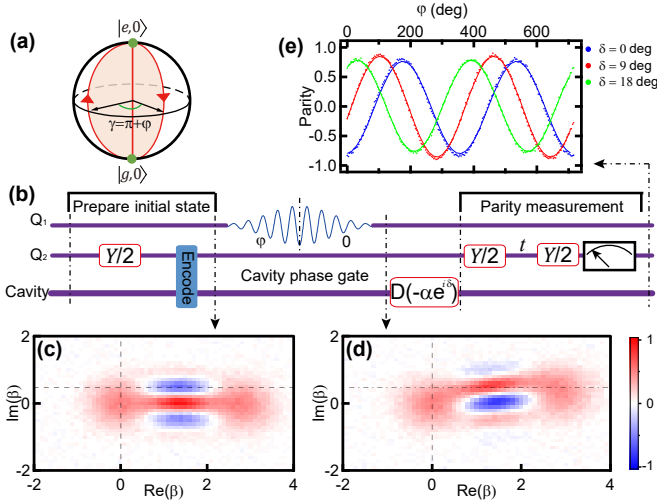


FIG. 1: Geometric manipulation of a photonic cat state. (a) Schematic of the nonadiabatic AA phase of a qubit. Two successive π rotations of the qubit produce a geometric phase $\gamma = \pi + \varphi$, where φ is the angle between the two rotation axes. (b) Experimental sequence to manipulate the cat state. A cavity is dispersively coupled to the qubit and initialized in a cat state $(|0\rangle + |2\alpha\rangle_c)/\sqrt{2}$ with the help of an ancillary qubit Q_2 . The AA phase produced by the rotations of Q_1 conditional on the cavity's vacuum state is encoded in the probability amplitude of $|0\rangle$, resulting in a phase gate. (c) Measured Wigner function of the cavity state before the phase gate, corresponding to fidelity of 0.980 to the ideal cat state. (d) Wigner function of the cavity state after the gate with $\varphi = 0$. The slight rotation and deformation of the Wigner function is due to the self-Kerr effect of the cavity. (e) Measured parity of the cavity state as a function of φ after a displacement $D(-\alpha e^{i\delta})$ for different values of δ . Symbols are experimental data, in excellent agreement with numerical simulations (solid lines).

Ref. [36]. Device B, on which two-cavity geometric phase gates are performed, consists of three transmon qubits dispersively coupled to two cylindrical cavities [37] and three stripline readout cavities [38]. The device parameters are described in Ref. [39]. In Device A, the coupling between the qubit (Q_1) used to produce the geometric phase and the cavity used to encode this phase is described by the Hamiltonian

$$H = -\hbar\chi_{\text{qs}}a^\dagger a|e\rangle\langle e|, \quad (1)$$

where χ_{qs} denotes the qubit frequency shift induced by per photon, a^\dagger and a are the creation and annihilation operators for the particular cavity field respectively, and $|e\rangle$ ($|g\rangle$) is the excited (ground) state of the qubit. In Device B, the qubit, commonly coupled to two cavities used to store the photonic qubits, undergoes a frequency shift dependent on the photon numbers of both cavities.

The geometric manipulation technique is well exemplified with the even cat state $(|\alpha\rangle_c + |-\alpha\rangle_c)/\sqrt{2}$, where $|\alpha\rangle_c$ and $|-\alpha\rangle_c$ are coherent states with $\langle\alpha|-\alpha\rangle \approx O(e^{-2|\alpha|^2})$. To realize conditional qubit rotations, a phase-space displacement, $D(\alpha)$, is applied to the cavity, transforming its state to $(|2\alpha\rangle_c + |0\rangle)/\sqrt{2}$. The qubit, initially in the ground state $|g\rangle$,

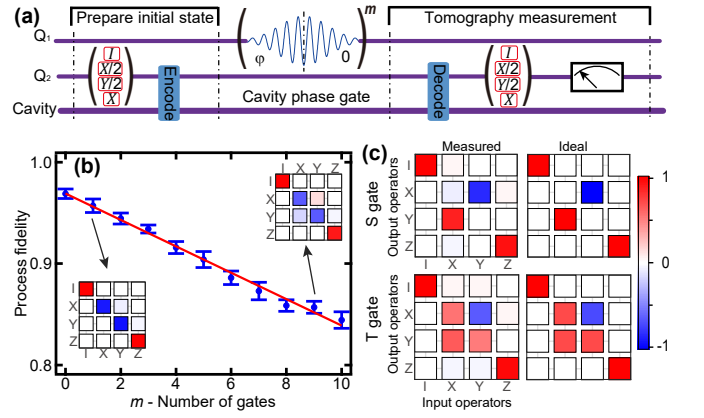


FIG. 2: Quantum process tomography (QPT) of single-cavity geometric phase gates. (a) Experimental sequence. (b) The Pauli transfer process R matrix fidelity as a function of m , the number of the Z gate on the cavity state. The inserts show the measured R matrices after one and nine Z gates, respectively. A linear fit of the process fidelity decay gives the Z gate fidelity $F_Z = 0.987 \pm 0.001$. (c) The measured and ideal Pauli transfer R matrices of the S gate and T gate with fidelities $F_S = 0.968$ and $F_T = 0.964$.

is then driven by a classical field on resonance with the qubit frequency conditioned on the cavity's vacuum state $|0\rangle$. We here assume that the Rabi frequency ε of the drive is much smaller than $\bar{n}\chi_{\text{qs}}$, where $\bar{n} = 4|\alpha|^2$ is the average photon number of the state $|2\alpha\rangle_c$. In this case, the qubit's state is not changed by the drive when the cavity is in $|2\alpha\rangle_c$ due to the large detuning, and the system dynamics is described by the effective Hamiltonian

$$H_{\text{eff}} = \frac{1}{2}\hbar\varepsilon e^{i\phi}|e\rangle\langle g| \otimes |0\rangle\langle 0| + h.c., \quad (2)$$

where ϕ is the phase of the drive. This Hamiltonian produces a qubit rotation $R_{\mathbf{n}}^\theta$ conditional on the cavity's vacuum state, where $R_{\mathbf{n}}^\theta$ represents the operation that rotates the qubit's state by an angle $\theta = \int_0^\tau \varepsilon dt$ around the axis \mathbf{n} with an angle ϕ to x axis on the equatorial plane of the Bloch sphere, with τ being the pulse duration.

After two successive conditional π rotations $R_{\mathbf{n}_1}^{\pi,0} = R_{\mathbf{n}_1}^\pi \otimes |0\rangle\langle 0|$ and $R_{\mathbf{n}_2}^{\pi,0} = R_{\mathbf{n}_2}^\pi \otimes |0\rangle\langle 0|$, the qubit makes a cyclic evolution, returning to the initial state $|g\rangle$ but acquiring a phase $\gamma = \pi + \Delta\phi = \Omega/2$, where $\Delta\phi = \phi_1 - \phi_2$ represents the angle between the two rotation axes, and Ω is the solid angle subtended by the trajectory traversed by the qubit on the Bloch sphere, as shown in Fig. 1(a). This conditional phase shift is encoded in the probability amplitude of the state component $|0\rangle$, leading to the cavity state $(|2\alpha\rangle_c + e^{i\gamma}|0\rangle)/\sqrt{2}$. A subsequent displacement $D(-\alpha)$ transforms the cavity to the state $(|\alpha\rangle_c + e^{i\gamma}|-\alpha\rangle_c)/\sqrt{2}$. Due to the quantum interference of the two superposed coherent state components $|\alpha\rangle_c$ and $|-\alpha\rangle_c$, the cavity parity P exhibits a periodical oscillation when the geometric phase γ is varied: $P = \cos \gamma$. The procedure allows for manipulation of the parity of the cat state; when $\gamma = \pi$, the parity is reversed. This procedure is equiv-

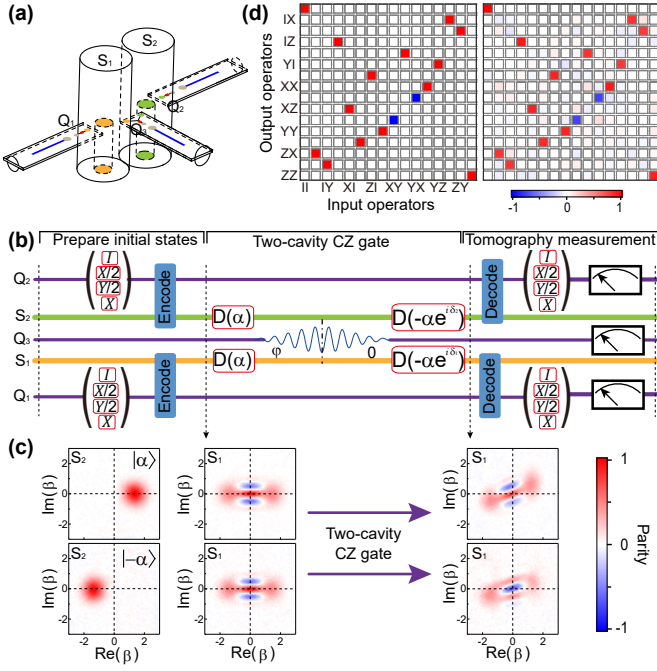


FIG. 3: Two-cavity geometric phase gate. (a) A 3D view of Device B. A superconducting transmon qubit Q_3 at the center couples to two coaxial cavities S_1 and S_2 , which couple to two other individual ancillary transmon qubits Q_1 and Q_2 , respectively. Each of these transmon qubits independently couples to a stripline readout resonator used to perform simultaneous single-shot readout. (b) Schematic of the experimental sequence. (c) Measured individual Wigner functions of storage cavity S_1 and S_2 . When the control cavity S_2 prepared in $|\alpha\rangle_c$ ($|- \alpha\rangle_c$), the even cat state $(|\alpha\rangle_c + |- \alpha\rangle_c)/\sqrt{2}$ in target cavity S_1 evolves to even (odd) cat state under the two-cavity CZ gate. The slight rotation and deformation of the Wigner functions after gate are due to the Kerr effect of the cavities. (d) Ideal (left) and measured (right) Pauli transfer R matrices of the two-cavity CZ gate with the coherent encoding $\{|0\rangle_L = |\alpha\rangle_c, |1\rangle_L = |- \alpha\rangle_c\}$. The corresponding process fidelity $F_{CZ,ED}$ (F_{ED}) is 0.859 (0.954).

alent to a phase gate operation for the cavity qubit with $|\alpha\rangle_c$ and $|- \alpha\rangle_c$ acting as the logical basis states, and can be used to correct for the parity jump caused by single-photon loss.

To simplify the operation, in our experiment the cavity displacement before the conditional qubit rotation is incorporated with the preparation of the initial cavity state; $|2\alpha\rangle_c$ ($\alpha = \sqrt{2}$) and $|0\rangle$ instead act as the two logical basis states $|0\rangle_L$ and $|1\rangle_L$ for the single-cavity phase gate demonstration. The experimental sequence to manipulate a cat state with Device A is shown in Fig. 1(b). The cavity is initialized in the cat state $(|2\alpha\rangle_c + |0\rangle)/\sqrt{2}$ [the measured Wigner function is shown in Fig. 1(c)] with the help of ancillary qubit Q_2 following the gradient ascent pulse engineering (GRAPE) technique [40, 41]. The two subsequent conditional π rotations on Q_1 , with the first one around the axis with an angle φ to the x axis and the second one around the x axis, yield a geometric phase $\gamma = \pi + \varphi$ conditional on the cavity's vacuum state. The Wigner function of the cavity state after this single-cavity geometric phase gate is shown in Fig. 1(d) with $\varphi = 0$,

which demonstrates the phase-space interference fringes are reversed by the geometric manipulation. After a displacement $D(-\alpha e^{i\delta})$, the parity of the cavity state as a function of φ is measured and shown in Fig. 1(e), in excellent agreement with numerical simulations.

Quantum process tomography (QPT) is used to benchmark the cavity geometric phase gate performance, with the experimental sequence shown in Fig. 2(a). Since trusted operations and measurements necessary for QPT are unavailable in the coherent-state-encoded subspace, we characterize the gate by decoding the quantum information on the cavity back to the transmon qubit Q_2 . We use the so-called Pauli transfer process R matrix as a measure of our gate [42], which connects the input and output Pauli operators with $P_{\text{out}} = R \cdot P_{\text{in}}$. Figure 2(b) shows the R matrix fidelity decay as a function of m , the number of the π -phase (Z) gate. The fidelity at $m = 0$ quantifies the ‘‘round trip’’ process fidelity $F_{ED} = 0.969$ of the encoding and decoding processes only. A linear fit of the process fidelity decay gives the Z gate fidelity $F_Z = 0.987$, also consistent with the fidelity calculated from $F_Z = 1 - (F_{ED} - F_{Z,ED})$, where $F_{Z,ED} = 0.957$ is the measured fidelity including the encoding and decoding processes. The measured and the ideal Pauli transfer R matrices of the S gate and T gate are shown in Fig. 2(c), where $S = |0\rangle_L \langle 0| + i|1\rangle_L \langle 1|$ and $T = |0\rangle_L \langle 0| + \exp(i\pi/4)|1\rangle_L \langle 1|$.

Our method can be directly generalized to implementation of controlled-phase gates between two photonic qubits encoded in two cavities that are dispersively coupled to one common superconducting qubit [43, 44]. Figure 3 shows the two-cavity geometric phase gates based on Device B, whose schematic is shown in Fig. 3(a). Besides the transmon qubit commonly connected to both cavities, each cavity is individually coupled to another ancillary transmon qubit for encoding/decoding and measurement purposes. A two-cavity CZ gate with the coherent state encoding $\{|0\rangle_L = |\alpha\rangle_c, |1\rangle_L = |- \alpha\rangle_c\}$ for both cavities is implemented by sandwiching a conditional qubit rotation between two pairs of displacement operations. The first pair of displacements transform the coherent states $|\alpha\rangle_c$ and $|- \alpha\rangle_c$ of each cavity to $|2\alpha\rangle_c$ and $|0\rangle$, respectively. The subsequent pulse, applied to the common qubit, produces a 2π rotation conditional on each cavity being in the vacuum state. The second pair of displacements restore each coherent state to the original amplitude. Consequently, the two cavities undergo a π phase shift if and only if they are both in the logical state $|1\rangle_L$.

Here, we use the two-cavity QPT method to benchmark the performance of our realized CZ gate, with the experimental sequence shown in Fig 3(b). We first prepare the two cavities in a product state $|0\rangle_L(|0\rangle_L + |1\rangle_L)/\sqrt{2}$ or $|1\rangle_L(|0\rangle_L + |1\rangle_L)/\sqrt{2}$ in two separate experiments. After performing the two-cavity CZ gate, the even cat state $(|\alpha\rangle_c + |- \alpha\rangle_c)/\sqrt{2}$ in the target cavity S_1 evolves to even (odd) cat state when the control cavity S_2 prepared in $|0\rangle_L$ ($|1\rangle_L$), which is verified by the Wigner functions of the target cavity S_1 measured before and after the two-cavity CZ gate as shown in Fig 3(c).

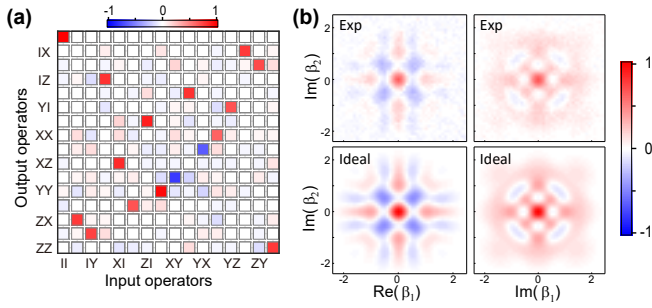


FIG. 4: Two-cavity CZ gate with binomial encoding. (a) Measured Pauli transfer R matrix of the two-cavity CZ gate with the binomial encoding. The corresponding process fidelity $F_{\text{CZ,ED}}$ (F_{ED}) is 0.816 (0.922). (b) The measured and ideal joint Wigner function of the generated entangled logical Bell state $|\Phi_+\rangle = (|01\rangle_L + |10\rangle_L)/\sqrt{2}$ on the Im-Re and Im-Im planes, respectively.

With the two-cavity QPT method, we fully characterize the realized CZ gate with the measured Pauli transfer R matrix, together with that for the ideal CZ gate, displaced in Fig. 3(d). The obtained process R matrix fidelities, $F_{\text{CZ,ED}}$ and F_{ED} , are respectively 0.859 and 0.954, which indicate the intrinsic two-cavity CZ gate fidelity is $F_{\text{CZ}} = 0.905$, with the infidelities mainly coming from the control pulse imperfections [39].

Our method allows implementation of a gate between two error-correctable logical qubits. For logical qubits whose basis states are encoded in even cat states, the photon-number parity can be used as an error syndrome of the single-photon loss [21–23]. With this encoding, each of the two-qubit logical basis states is composed of four two-mode coherent state components, and a CZ gate can be realized by subsequently performing four conditional phase operations. Each operation inverts the phase of one of the four components forming a specific logical basis state, and can be realized by sandwiching a qubit 2π rotation conditional on the cavities' vacuum state between two pairs of phase-space displacements of the cavities. We note that the displacement used to transform one coherent state to the vacuum state will move the corresponding logical qubit out of the error-correctable logical space. This problem can be overcome with another kind of error-correctable logical qubits binomially encoded as $\{|0\rangle_L = (|0\rangle + |4\rangle_F)/\sqrt{2}, |1\rangle_L = |2\rangle_F\}$ [45, 46].

To demonstrate the applicability of our method to binomial logical qubits, we first binomially encode the two cavities, then perform a CZ gate between thus-encoded qubits via geometric manipulation, and finally read out their joint state. The experimental sequence is similar to that in Fig. 3(b) but without the displacements. Due to the limitation of the dispersive couplings between the ancilla qubit and the cavities, the drive tuned to the ancilla's frequency associated with the cavities' basis state $|22\rangle_F$ will off-resonantly couple the ancilla's $|g\rangle$ and $|e\rangle$ states, and thus produce a small dynamical phase when the cavities are in other joint photon-number states. To minimize this dynamical effect and to speed up the gate, we successively apply two π pulses to the ancilla: the first one

has a duration of 20 ns and is nonselective; while the second one has a duration of $2\ \mu\text{s}$ and involves nine frequency components, each selective on one of the following nine joint Fock states $|j,k\rangle_F$ ($j, k = 0, 2, 4$). With suitable choice of the amplitudes and phases of these driving components, the resulting phase shift associated with the logical state $|22\rangle_F$ differs from those with other joint Fock states by π .

The two-cavity QPT method is also used here to benchmark the realized CZ gate with the binomial encoding, and the measured corresponding Pauli transfer R matrix is displayed in Fig. 4(a). The corresponding process fidelity $F_{\text{CZ,ED}}$ (F_{ED}) obtained from the measured R matrix is 0.816 (0.922), which indicates the intrinsic CZ gate fidelity $F_{\text{CZ}} = 0.894$. We note that during the gate operation, it is unnecessary to change the photon numbers for both cavities, so that they remain in the original logical space.

Combined with additional single-cavity Hadamard gates of the binomial logical qubits realized by using the GRAPE technique, our two-cavity CZ gate can be used to directly generate entangled logical Bell state $|\Phi_+\rangle = (|01\rangle_L + |10\rangle_L)/\sqrt{2}$. With help of the two ancillary qubits, joint Wigner tomography of the generated Bell state is performed. The upper row of Fig. 4(b) displays the two slice cuts of the measured two-mode Wigner functions for the generated Bell state, which agree well with those for the ideal logical Bell state shown in the lower row in Fig. 4(b). The fidelity of this entangled state, measured by decoding the logical states back to the ancillary qubits and then performing a joint state tomography, is 0.861.

Besides the controlled-phase gates, the geometric dynamics can be used to realize two-cavity SNAP gate, which represents an extension of the previously reported SANP operation for universal control of a single cavity state [39]. The method can also be directly generalized to realize geometric gates among three or more cat- or binomially-encoded qubits by properly setting the driving pulse. This kind of gates is useful for quantum error correction [47] and serves as a central element for implementation of the quantum search algorithm [48].

We thank valuable discussions with Chen Wang and Chang-Ling Zou. This work was supported by National Key Research and Development Program of China No.2017YFA0304303 and the National Natural Science Foundation of China under Grants No.11474177, No. 11874114, No. 11674060, and No. 11875108.

* These two authors contributed equally to this work.

† Electronic address: zbyang@fzu.edu.cn

‡ Electronic address: t96034@fzu.edu.cn

§ Electronic address: luyansun@tsinghua.edu.cn

- [1] J. Anandan, "The geometric phase," *Nature* **360**, 307 (1992).
- [2] F. Wilczek and A. Shapere, *Geometric Phases in Physics* (WORLD SCIENTIFIC, 1989).
- [3] M. V. Berry, "Quantal phase factors accompanying adiabatic changes," *Proc. R. Soc. Lond.* **392**, 45 (1984).
- [4] G. De Chiara and G. M. Palma, "Berry phase for a spin 1/2 par-

- title in a classical fluctuating field,” *Phys. Rev. Lett.* **91**, 090404 (2003).
- [5] L. Duan, J. I. Cirac, and P. Zoller, “Geometric manipulation of trapped ions for quantum computation,” *Science* **292**, 1695 (2001).
- [6] J. A. Jones, V. Vedral, A. Ekert, and G. Castagnoli, “Geometric quantum computation using nuclear magnetic resonance,” *Nature* **403**, 869 (2000).
- [7] R. Tycko, “Adiabatic rotational splittings and berry’s phase in nuclear quadrupole resonance,” *Phys. Rev. Lett.* **58**, 2281 (1987).
- [8] P. J. Leek, J. M. Fink, A. Blais, R. Bianchetti, M. Göppl, J. M. Gambetta, D. I. Schuster, L. Frunzio, R. J. Schoelkopf, and A. Wallraff, “Observation of berry’s phase in a solid-state qubit,” *Science* **318**, 1889 (2007).
- [9] S. Filipp, J. Klepp, Y. Hasegawa, C. Plonka-Spehr, U. Schmidt, P. Geltenbort, and H. Rauch, “Experimental demonstration of the stability of berry’s phase for a spin-1/2 particle,” *Phys. Rev. Lett.* **102**, 030404 (2009).
- [10] M. Pechal, S. Berger, A. A. Abdumalikov, J. M. Fink, J. A. Mlynek, L. Steffen, A. Wallraff, and S. Filipp, “Geometric phase and nonadiabatic effects in an electronic harmonic oscillator,” *Phys. Rev. Lett.* **108**, 170401 (2012).
- [11] S. Gasparinetti, S. Berger, A. A. Abdumalikov, M. Pechal, S. Filipp, and A. J. Wallraff, “Measurement of a vacuum-induced geometric phase,” *Sci. Adv.* **2**, e1501732 (2016).
- [12] Y. Aharonov and J. Anandan, “Phase change during a cyclic quantum evolution,” *Phys. Rev. Lett.* **58**, 1593 (1987).
- [13] J. Samuel and R. Bhandari, “General setting for berry’s phase,” *Phys. Rev. Lett.* **60**, 2339 (1988).
- [14] S.-B. Zheng, “Unconventional geometric quantum phase gates with a cavity qed system,” *Phys. Rev. A* **70**, 052320 (2004).
- [15] D. Leibfried, B. DeMarco, V. Meyer, D. Lucas, M. Barrett, J. Britton, W. M. Itano, B. Jelenković, C. Langer, T. Rosenband, *et al.*, “Experimental demonstration of a robust, high-fidelity geometric two ion-qubit phase gate,” *Nature* **422**, 412 (2003).
- [16] C. Song, S.-B. Zheng, P. Zhang, K. Xu, L. Zhang, Q. Guo, W. Liu, D. Xu, H. Deng, K. Huang, D. Zheng, X. Zhu, and H. Wang, “Continuous-variable geometric phase and its manipulation for quantum computation in a superconducting circuit,” *Nat. Commun.* **8**, 1061 (2017).
- [17] S. Krastanov, V. V. Albert, C. Shen, C.-L. Zou, R. W. Heeres, B. Vlastakis, R. J. Schoelkopf, and L. Jiang, “Universal control of an oscillator with dispersive coupling to a qubit,” *Phys. Rev. A* **92**, 040303 (2015).
- [18] R. W. Heeres, B. Vlastakis, E. Holland, S. Krastanov, V. V. Albert, L. Frunzio, L. Jiang, and R. J. Schoelkopf, “Cavity state manipulation using photon-number selective phase gates,” *Phys. Rev. Lett.* **115**, 137002 (2015).
- [19] S. Rosenblum, Y. Y. Gao, P. Reinhold, C. Wang, C. J. Axline, L. Frunzio, S. M. Girvin, L. Jiang, M. Mirrahimi, M. H. Devoret, and R. J. Schoelkopf, “A CNOT gate between multi-photon qubits encoded in two cavities,” *Nat. Commun.* **9**, 652 (2018).
- [20] S. Deléglise, I. Dotsenko, C. Sayrin, J. Bernu, M. Brune, J. M. Raimond, and S. Haroche, “Reconstruction of non-classical cavity field states with snapshots of their decoherence,” *Nature* **455**, 510 (2008).
- [21] Z. Leghtas, G. Kirchmair, B. Vlastakis, R. J. Schoelkopf, M. H. Devoret, and M. Mirrahimi, “Hardware-efficient autonomous quantum memory protection,” *Phys. Rev. Lett.* **111**, 120501 (2013).
- [22] M. Mirrahimi, Z. Leghtas, V. V. Albert, S. Touzard, R. J. Schoelkopf, L. Jiang, and M. H. Devoret, “Dynamically protected cat-qubits: a new paradigm for universal quantum computation,” *New J. Phys.* **16**, 045014 (2014).
- [23] N. Ofek, A. Petrenko, R. Heeres, P. Reinhold, Z. Leghtas, B. Vlastakis, Y. Liu, L. Frunzio, S. M. Girvin, L. Jiang, M. Mirrahimi, M. H. Devoret, and R. J. Schoelkopf, “Extending the lifetime of a quantum bit with error correction in superconducting circuits,” *Nature* **536**, 441 (2016).
- [24] R. Heeres, P. Reinhold, N. Ofek, L. Frunzio, L. Jiang, M. H. Devoret, and R. J. Schoelkopf, “Implementing a universal gate set on a logical qubit encoded in an oscillator,” *Nat. Commun.* **8**, 94 (2017).
- [25] L. Sun, A. Petrenko, Z. Leghtas, B. Vlastakis, G. Kirchmair, K. M. Sliwa, A. Narla, M. Hatridge, S. Shankar, J. Blumoff, L. Frunzio, M. Mirrahimi, M. H. Devoret, and R. J. Schoelkopf, “Tracking photon jumps with repeated quantum non-demolition parity measurements,” *Nature* **511**, 444 (2014).
- [26] A. Wallraff, D. I. Schuster, A. Blais, L. Frunzio, R.-S. Huang, J. Majer, S. Kumar, S. M. Girvin, and R. J. Schoelkopf, “Strong coupling of a single photon to a superconducting qubit using circuit quantum electrodynamics,” *Nature* **431**, 162 (2004).
- [27] J. Clarke and F. K. Wilhelm, “Superconducting quantum bits,” *Nature* **453**, 1031 (2008).
- [28] J. Q. You and F. Nori, “Atomic physics and quantum optics using superconducting circuits,” *Nature* **474**, 589 (2011).
- [29] M. H. Devoret and R. J. Schoelkopf, “Superconducting circuits for quantum information: An outlook,” *Science* **339**, 1169 (2013).
- [30] X. Gu, A. F. Kockum, A. Miranowicz, Y. X. Liu, and F. Nori, “Microwave photonics with superconducting quantum circuits,” *Phys. Rep.* **718-719**, 1 (2017).
- [31] H. Paik, D. I. Schuster, L. S. Bishop, G. Kirchmair, G. Cate-lani, A. P. Sears, B. R. Johnson, M. J. Reagor, L. Frunzio, L. I. Glazman, S. M. Girvin, M. H. Devoret, and R. J. Schoelkopf, “Observation of high coherence in josephson junction qubits measured in a three-dimensional circuit qed architecture,” *Phys. Rev. Lett.* **107**, 240501 (2011).
- [32] G. Kirchmair, B. Vlastakis, Z. Leghtas, S. E. Nigg, H. Paik, E. Ginossar, M. Mirrahimi, L. Frunzio, S. M. Girvin, and R. J. Schoelkopf, “Observation of quantum state collapse and revival due to the single-photon Kerr effect,” *Nature* **495**, 205 (2013).
- [33] B. Vlastakis, G. Kirchmair, Z. Leghtas, S. E. Nigg, L. Frunzio, S. M. Girvin, M. Mirrahimi, M. H. Devoret, and R. J. Schoelkopf, “Deterministically encoding quantum information using 100-photon Schrödinger cat states,” *Science* **342**, 607 (2013).
- [34] K. Liu, Y. Xu, W. Wang, S.-B. Zheng, T. Roy, S. Kundu, M. Chand, A. Ranadive, R. Vijay, Y. Song, *et al.*, “A twofold quantum delayed-choice experiment in a superconducting circuit,” *Sci. Adv.* **3**, e1603159 (2017).
- [35] W. Wang, L. Hu, Y. Xu, K. Liu, Y. Ma, S.-B. Zheng, R. Vijay, Y. P. Song, L.-M. Duan, and L. Sun, “Converting quasiclassical states into arbitrary fock state superpositions in a superconducting circuit,” *Phys. Rev. Lett.* **118**, 223604 (2017).
- [36] Y. Xu, W. Cai, Y. Ma, X. Mu, L. Hu, T. Chen, H. Wang, Y. P. Song, Z.-Y. Xue, Z.-q. Yin, and L. Sun, “Single-loop realization of arbitrary nonadiabatic holonomic single-qubit quantum gates in a superconducting circuit,” *Phys. Rev. Lett.* **121**, 110501 (2018).
- [37] M. Reagor, W. Pfaff, C. Axline, R. W. Heeres, N. Ofek, K. Sliwa, E. Holland, C. Wang, J. Blumoff, K. Chou, M. J. Hatridge, L. Frunzio, M. H. Devoret, L. Jiang, and R. J. Schoelkopf, “Quantum memory with millisecond coherence in circuit qed,” *Phys. Rev. B* **94**, 014506 (2016).
- [38] C. Axline, M. Reagor, R. Heeres, P. Reinhold, C. Wang,

- K. Shain, W. Pfaff, Y. Chu, L. Frunzio, and R. J. Schoelkopf, “An architecture for integrating planar and 3D cQED devices,” *Appl. Phys. Lett.* **109**, 042601 (2016).
- [39] Supplementary Materials .
- [40] N. Khaneja, T. Reiss, C. Kehlet, T. Schulte-Herbrüggen, and S. J. Glaser, “Optimal control of coupled spin dynamics: design of NMR pulse sequences by gradient ascent algorithms,” *J. Magn. Reson.* **172**, 296 (2005).
- [41] P. de Fouquieres, S. Schirmer, S. Glaser, and I. Kuprov, “Second order gradient ascent pulse engineering,” *J. Magn. Reson.* **212**, 412 (2011).
- [42] J. M. Chow, J. M. Gambetta, A. D. Córcoles, S. T. Merkel, J. A. Smolin, C. Rigetti, S. Poletto, G. A. Keefe, M. B. Rothwell, J. R. Rozen, M. B. Ketchen, and M. Steffen, “Universal quantum gate set approaching fault-tolerant thresholds with superconducting qubits,” *Phys. Rev. Lett.* **109**, 060501 (2012).
- [43] C. Wang, Y. Y. Gao, P. Reinhold, R. W. Heeres, N. Ofek, K. Chou, C. Axline, M. Reagor, J. Blumoff, K. Sliwa, *et al.*, “A schrödinger cat living in two boxes,” *Science* **352**, 1087 (2016).
- [44] Y. Y. Gao, B. J. Lester, K. S. Chou, L. Frunzio, M. H. Devoret, L. Jiang, S. M. Girvin, and R. J. Schoelkopf, “Entanglement of bosonic modes through an engineered exchange interaction,” *Nature* **566**, 509 (2019).
- [45] M. H. Michael, M. Silveri, R. T. Brierley, V. V. Albert, J. Salmilehto, L. Jiang, and S. M. Girvin, “New class of quantum error-correcting codes for a bosonic mode,” *Phys. Rev. X* **6**, 031006 (2016).
- [46] L. Hu, Y. Ma, W. Cai, X. Mu, Y. Xu, W. Wang, Y. Wu, H. Wang, Y. Song, C. Zou, S. M. Girvin, L.-M. Duan, and L. Sun, “Quantum error correction and universal gate set on a binomial bosonic logical qubit,” *Nat. Phys.* **15**, 503 (2019).
- [47] M. D. Reed, L. DiCarlo, S. E. Nigg, L. Sun, L. Frunzio, S. M. Girvin, and R. J. Schoelkopf, “Realization of three-qubit quantum error correction with superconducting circuits,” *Nature* **482**, 382 (2012).
- [48] M. A. Nielsen and I. L. Chuang, *Quantum Computation and Quantum Information* (Cambridge Univ. Press, 2000).

Supplementary Material for “Geometrically manipulating photonic Schrödinger cat states and realizing two-logical-qubit gates”

Y. Xu,^{1,*} Y. Ma,^{1,*} W. Cai,¹ X. Mu,¹ W. Dai,¹ W. Wang,¹ L. Hu,¹ X. Li,¹ J. Han,¹
H. Wang,¹ Y. P. Song,¹ Zhen-Biao Yang,^{2,†} Shi-Biao Zheng,^{2,‡} and L. Sun^{1,§}

¹Center for Quantum Information, Institute for Interdisciplinary Information Sciences, Tsinghua University, Beijing 100084, China

²Fujian Key Laboratory of Quantum Information and Quantum Optics,
College of Physics and Information Engineering, Fuzhou University, Fuzhou, Fujian 350108, China

I. EXPERIMENTAL DEVICE AND SETUP

The single-cavity geometric phase gates are performed on Device A, which consists of two transmon qubits simultaneously dispersively coupled to two three-dimensional (3D) cavities [1–5]. Details of the device parameters and architecture setup are described in Ref. [6]. Here we only describe Device B in detail.

Device B with a circuit quantum electrodynamics (cQED) architecture contains two 3D coaxial stub cavities (S_1 and S_2), three superconducting transmon qubits (Q_1 , Q_2 , and Q_3), and three stripline readout resonators (R_1 , R_2 , and R_3). The 3D view of Device B is shown in Fig. 3(a) of the main text and the optical image is shown in Fig. S1. The device is machined from a block of high-purity (5N5) aluminum and is chemically etched to improve the surface quality [7]. The two coaxial cavities are 3D $\lambda/4$ transmission line resonators [8–10] with a center conductor of 3.3 mm in diameter and a cylindrical wall of 9.6 mm in diameter. The fundamental mode frequencies are mainly determined by the heights of the center stubs, 9.8 mm and 10.8 mm for S_1 and S_2 respectively. There are three horizontal tunnels housing three individual sapphire chips with patterned transmon qubits to couple to the two cavity modes. Qubit Q_3 on the middle chip is designed with three antenna pads to couple to the two coaxial cavity modes and

one stripline readout mode, respectively. Each of the other two ancillary qubits (Q_1 and Q_2) only has two antenna pads to couple to the corresponding cavity mode and individual stripline readout resonator. Each stripline readout resonator is formed by the metal wall of the tunnel and an aluminum strip simultaneously patterned on the same chip with the transmon qubit through a standard double-angle evaporation process after a single electron-beam lithography step.

The device is anchored to the mixing chamber of a cryogen-free dilution refrigerator which is cooled down to $T \approx 10$ mK. An additional magnetic shield covering the device is used to provide a clean electromagnetic environment. Attenuators and low-pass filters are used on the microwave lines to reduce the radiation noises of the signals. All the qubit and cavity drives are generated by IQ modulations with two analog channels of a Tektronix AWG5014C and an IQ mixer. The cavity states are initialized with the help of the ancillary qubits following the gradient ascent pulse engineering (GRAPE) technique [11, 12]. The qubit control pulses have a truncated Gaussian envelope with a width of $4\sigma = 20$ ns. With the technique of “derivative removal by adiabatic gate” (DRAG) to remove the leakage and phase errors of the drive pulses [13, 14], the single qubit gates, characterized by the randomized benchmarking (RB) method [15–19], result in an average fidelity of 0.9990, 0.9986, and 0.9992 for the three qubits respectively. The three qubits can be simultaneously measured with three individual readout control signals generated with different modulations of a same local oscillator (LO). The readout signals are first amplified by quantum limited amplifiers at base temperature. We use two separate Josephson parametric amplifiers (JPA) for Q_1 and Q_2 , and a Josephson parametric converter (JPC) for Q_3 . Each readout signal is further amplified by a high electron mobility transistor (HEMT) at 4K stage and a standard commercial RF amplifier at room temperature. Finally, the three readout signals are combined together and mixed down with the LO. After being digitized and recorded by the analog-to-digital converters (ADC), the three readout signals can be distinguished through demodulations with different frequencies. The schematic of the full wiring of the experimental setup is shown in Fig. S2.

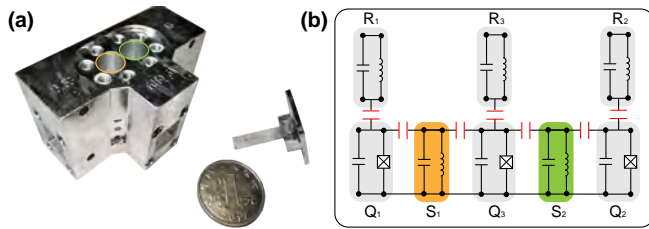


FIG. S1: (a) Optical image of Device B. The device is machined from a block of high-purity (5N5) aluminum and is chemically etched. It consists of two coaxial stub cavities and three transmon qubits on different individual sapphire chips in three separate horizontal tunnels. Each qubit also couples to an individual stripline readout resonator. (b) Schematic of the effective circuit of Device B.

II. SYSTEM HAMILTONIAN

The three transmon qubits are dispersively coupled to the corresponding 3D cavity modes. Each transmon has a large anharmonicity and is considered as a two-level artificial atom, while each cavity mode is considered as a harmonic oscillation.

*These two authors contributed equally to this work.

†Electronic address: zbyang@fzu.edu.cn

‡Electronic address: t96034@fzu.edu.cn

§Electronic address: luyansun@tsinghua.edu.cn

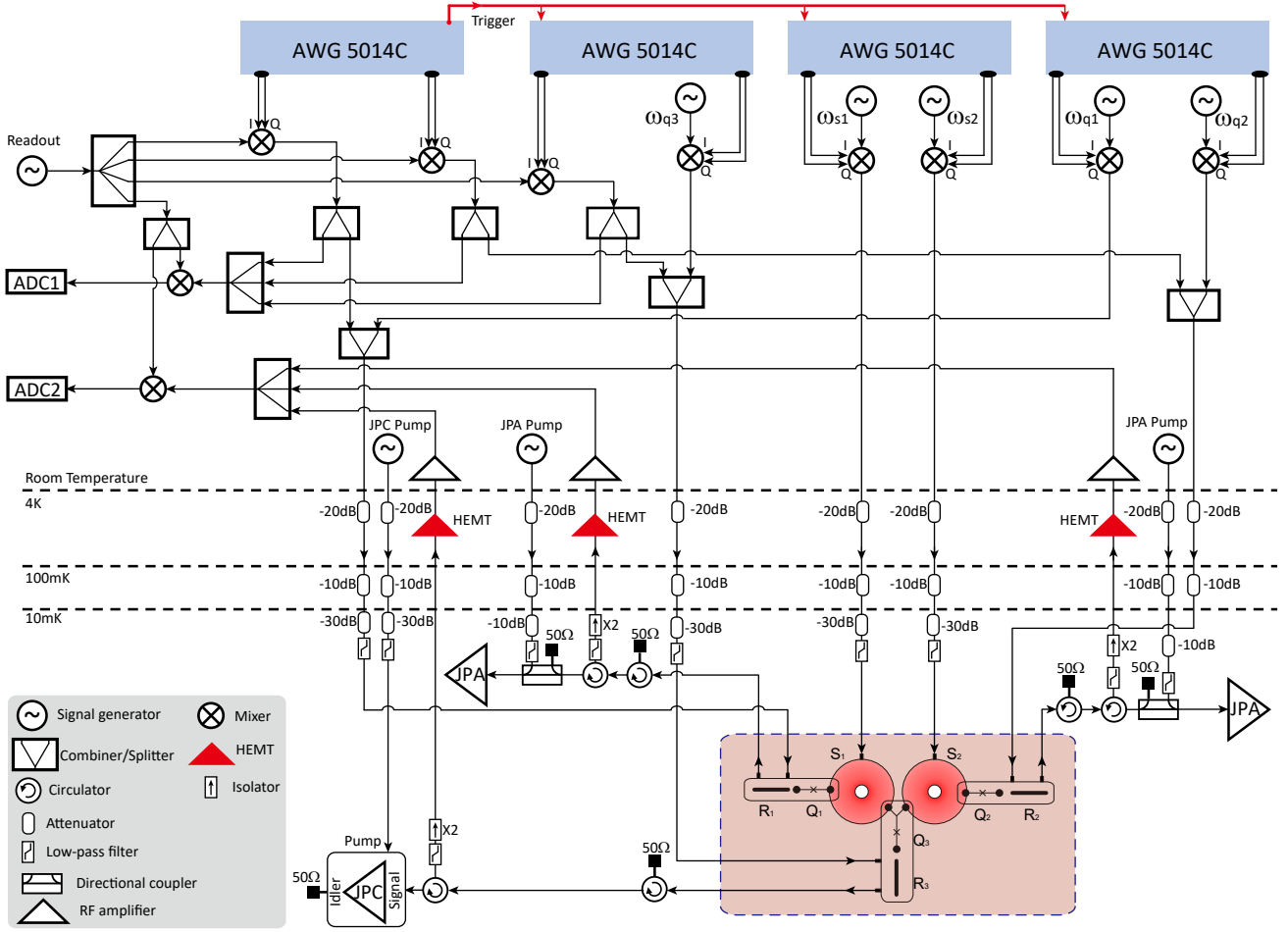


FIG. S2: Schematic of the full wiring of the experimental setup.

tor. Thus, the whole system can be described by the following Hamiltonian

$$\begin{aligned}
 \mathcal{H}/\hbar = & \sum_{i=1}^3 \omega_{ri} a_{ri}^\dagger a_{ri} + \sum_{i=1}^3 \omega_{qi} |e_i\rangle \langle e_i| + \sum_{i=1}^2 \omega_{si} a_{si}^\dagger a_{si} \\
 & - \sum_{i=1}^3 \chi_{rqi} |e_i\rangle \langle e_i| a_{ri}^\dagger a_{ri} \\
 & - \chi_{s1q1} |e_1\rangle \langle e_1| a_{s1}^\dagger a_{s1} - \chi_{s1q3} |e_3\rangle \langle e_3| a_{s1}^\dagger a_{s1} \\
 & - \chi_{s2q2} |e_2\rangle \langle e_2| a_{s2}^\dagger a_{s2} - \chi_{s2q3} |e_3\rangle \langle e_3| a_{s2}^\dagger a_{s2} \\
 & - \sum_{i=1}^2 \frac{K_{si}}{2} a_{si}^\dagger a_{si}^\dagger a_{si} a_{si} - \chi_{s1s2} a_{s1}^\dagger a_{s1} a_{s2}^\dagger a_{s2}, \quad (\text{S1})
 \end{aligned}$$

where ω_{ri} is the readout resonator frequency of the i -th qubit with the corresponding ladder operators a_{ri} and a_{ri}^\dagger ; ω_{si} are the resonant frequency of the i -th storage cavity with the corresponding ladder operators a_{si} and a_{si}^\dagger ; ω_{qi} is the transition frequency between the lowest two energy levels of the i -th qubit; χ_{rqi} is the dispersive interaction between the i -th qubit and its corresponding readout resonator; χ_{s1q1} , χ_{s1q3} , χ_{s2q2} , and χ_{s2q3} are the dispersive interactions between the three qubits and

the two storage cavity modes; K_{si} is the self-Kerr of the i -th storage cavity; and χ_{s1s2} is the cross-Kerr of the two storage cavities. All the relevant parameters in the Hamiltonian are experimentally measured and listed in Table S1.

The coherence properties of the qubits and the cavity modes are also experimentally characterized with the standard cQED measurements. In particular, the coherence times T_1 and T_2^* of the storage cavities are measured through the relaxing of the Fock state $|1\rangle$ and the dephasing of the superposition state $(|0\rangle + |1\rangle)/\sqrt{2}$, respectively [8]. Both initial states are generated with the selective number-dependent arbitrary phase (SNAP) gates [20]. All the results are listed in Table S2.

III. SIMULTANEOUS READOUT

In our experiment, each transmon qubit is connected to a quantum limited amplifier for fast high-fidelity single-shot readouts. The independence of the drives and measurements on them can be verified by simultaneous readouts of the two ancillary qubits, and the results are shown in Fig. S3.

In order to calibrate the three-qubit readout error, we prepare the system in each computational basis state

TABLE S1: Measured Hamiltonian parameters.

Modes	Frequency (GHz)	Nonlinear terms: $\chi_{ij}/2\pi$ (MHz)				
		S_1	S_2	Q_1	Q_2	Q_3
S_1	6.594	0.005	0.004	1.599	-	0.524
S_2	6.050	0.004	0.016	-	2.670	1.494
Q_1	6.038	1.599	-	252	-	-
Q_2	5.170	-	2.670	-	207	-
Q_3	5.560	0.524	1.494	-	-	151
R_1	8.892	-	-	2.0	-	-
R_2	8.800	-	-	-	2.0	-
R_3	9.032	-	-	-	-	1.5

TABLE S2: Coherence properties of the system.

Modes	T_1	T_2^*	T_2^{Echo}
S_1	480 μs	559 μs	-
S_2	692 μs	312 μs	-
Q_1	35 μs	25 μs	56.0 μs
Q_2	20 μs	12 μs	20 μs
Q_3	25 μs	25 μs	30 μs
R_1	58 ns	-	-
R_2	55 ns	-	-
R_3	86 ns	-	-

TABLE S3: Three-qubit simultaneous readout assignment probability matrix \mathcal{R} . Each column represents the three-qubit measurement probabilities after preparing the qubits in the corresponding computational basis state.

	$ ggg\rangle$	$ gge\rangle$	$ geg\rangle$	$ gee\rangle$	$ egg\rangle$	$ ege\rangle$	$ eeg\rangle$	$ eee\rangle$
000	95.2	4.0	7.8	0.3	5.9	0.2	0.5	0.0
001	0.8	92.4	0.1	7.5	0.1	4.8	0.0	0.4
010	2.1	0.1	89.9	3.7	0.1	0.0	6.3	0.2
011	0.0	2.0	0.8	87.1	0.0	0.1	0.1	4.4
100	1.8	0.1	0.1	0.0	91.2	3.6	7.3	0.3
101	0.0	1.5	0.0	0.1	0.7	89.3	0.1	7.2
110	0.0	0.0	1.4	0.0	1.9	0.1	85.0	3.4
111	0.0	0.0	0.0	1.2	0.0	1.9	0.8	84.0

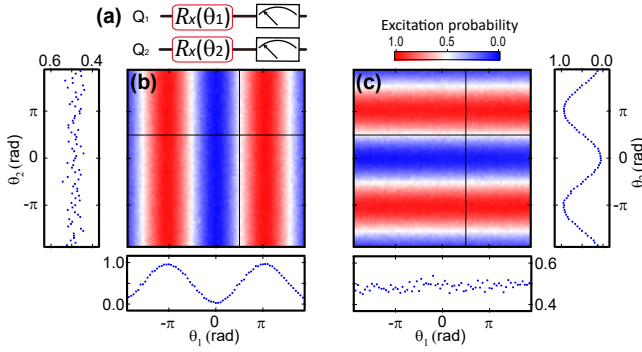


FIG. S3: Simultaneous Rabi experiments on the two ancillary qubits. (a) The experimental pulse sequence, where the two ancillary qubits are rotated along x axis with independent angles θ_1 and θ_2 , respectively, followed by simultaneous measurements on both of them. The measured excitation probabilities of qubits Q_1 and Q_2 as a function of the rotation angles θ_1 and θ_2 are shown in (b) and (c), respectively. The horizon and vertical cuts are also shown accordingly.

and simultaneously measure the assignment probability $\vec{p} = (p_{000}, p_{001}, p_{010}, p_{011}, p_{100}, p_{101}, p_{110}, p_{111})^T$ of the three qubits. By repeating the experiments for all the three-qubit computational basis states, we obtain the 8×8 readout matrix \mathcal{R} as shown in Table S3. We then can correct the readout errors by multiplying the inverse of the readout matrix \mathcal{R} with the measured probability \vec{p} , such that $\vec{p}_{\text{corr}} = \mathcal{R}^{-1} \cdot \vec{p}$ represents the real occupation probabilities of the eight computational basis states. For all the two-cavity experimental data shown in the main text, we have corrected the readout errors with this method.

IV. ENCODING AND DECODING PULSES

In our experiment, in order to make the preparation and characterization of the cavity states easier, we employ optimal control pulses to encode and decode the cavity states, facilitated by the corresponding adjacent ancillary qubit. The encoding/decoding process corresponds to a unitary operation to realize a state mapping between the ancillary qubit and the storage cavity.

To realize the encoding/decoding of storage cavity S_1 (S_2), we use the Hamiltonian defined in Eq. S1 (only considering the relevant qubit-cavity modes), together with the control terms on the ancillary qubit Q_1 (Q_2) and cavity S_1 (S_2) in the form $\varepsilon_q(t)\sigma^+ + \varepsilon_q(t)^*\sigma^-$ and $\varepsilon_s(t)a_s^\dagger + \varepsilon_s(t)^*a_s$, respectively. The temporal pulse envelopes $\varepsilon_q(t)$ and $\varepsilon_s(t)$ are discretized into 1 ns time step with piecewise constant, and numerically optimized with the quasi-Newton method to finally realize the target unitary U_{tar} .

In particular, for the encoding pulse, we wish to realize a unitary U_{EN} to perform the following state mapping:

$$(c_0|g\rangle + c_1|e\rangle)|0\rangle \xrightarrow{U_{\text{EN}}} |g\rangle(c_0|0\rangle_L + c_1|1\rangle_L), \quad (\text{S2})$$

for all complex amplitudes c_0 and c_1 with both the coherent state encoding $\{|0\rangle_L = |\alpha\rangle_c, |1\rangle_L = |-\alpha\rangle_c\}$ and the binomial encoding $\{|0\rangle_L = (|0\rangle + |4\rangle_F)/\sqrt{2}, |1\rangle_L = |2\rangle_F\}$. This unitary process maps the quantum information stored in the ancillary qubit onto a superposition of logical basis states encoded in the cavity, while the ancillary qubit returns to the ground state after the operation.

For the decoding process, it simply reverses the above process: mapping the quantum information encoded in the cavity state in a superposition of logical basis states back onto the ancillary qubit state, while the cavity returns to the vacuum state after the operation. The decoding pulse is also used to eliminate the deterministic rotation and deformation due to the self-Kerr term in Eq. S1. Therefore, after a geometric gate with a gate time T , the decoding pulse realizes the following state mapping:

$$|g\rangle \left\{ e^{i\frac{K_s}{2} a_s^\dagger a_s^\dagger a_s a_s T} (c_0 |0\rangle_L + c_1 |1\rangle_L) \right\} \xrightarrow{U_{DE}} (c_0 |g\rangle + c_1 |e\rangle) |0\rangle, \quad (\text{S3})$$

for all complex amplitudes c_0 and c_1 . In order to make the decoding process more accurate, we have used the density matrices obtained from master equation simulations to perform the state mapping and calculate the decoding pulses.

In our implementation, the encoding/decoding pulses are first numerically calculated with the gradient descent method to realize the target state mapping and further optimized in the experiment in order to achieve the highest process fidelity.

V. QUANTUM PROCESS TOMOGRAPHY

Both the single-cavity and two-cavity phase gates are characterized with full quantum process tomography (QPT) [21]. We first prepare the cavity state with the encoding pulse. After performing the geometric gates on the cavity state, the decoding pulse is applied to map the cavity state back to the ancillary qubit state, which is reconstructed with pre-rotations $\{I, X_{\pi/2}, Y_{\pi/2}, X_{\pi}\}$ on each ancillary qubit before measurements. The density matrix is then reconstructed by the maximum likelihood estimation method [22].

Here, we use the Pauli transfer matrix R to represent the quantum process, which is visually efficient and informative [23]. In order to characterize the quantum process, before the encoding process we use initial states $\{|g\rangle, |e\rangle, (|g\rangle + |e\rangle)/\sqrt{2}, (|g\rangle - i|e\rangle)/\sqrt{2}\}$ of the ancillary qubit for the single-cavity gates and $\{|g\rangle, |e\rangle, (|g\rangle + |e\rangle)/\sqrt{2}, (|g\rangle - i|e\rangle)/\sqrt{2}\}^{\otimes 2}$ of the ancillary qubits for the two-cavity gates. The R matrix maps the input state vector \vec{p}_{in} with the output state vector \vec{p}_{out} by $\vec{p}_{\text{out}} = R \cdot \vec{p}_{\text{in}}$. The process fidelity is calculated from the measured R matrix with

$$F = \frac{\text{Tr}(R^\dagger R_{\text{ideal}})/d + 1}{d + 1}, \quad (\text{S4})$$

where R_{ideal} is for a perfect process, $d = 2n$, and n is the number of cavities.

VI. JOINT WIGNER TOMOGRAPHY

We verify the quantum entanglement of the two-cavity states with the joint Wigner tomography [9], which is a measurement of the displaced joint photon number parity $P_J(\beta_1, \beta_2)$ of the two cavities. We simultaneously map the

parity of each cavity to its adjacent ancillary qubit. The single-shot readout of each qubit allows us to extract the displaced joint parity $P_J(\beta_1, \beta_2) = P_1(\beta_1)P_2(\beta_2)$ by multiplying the two individually displaced cavity parities $P_1(\beta_1)$ and $P_2(\beta_2)$.

The realized two-cavity geometric controlled-Z (CZ) gate can be effectively used for generating entangled two-cavity states. For example of the coherent state encoded logical qubits, we first prepare the two storage cavities in a product state of two cat states $|\psi_0\rangle = (|\alpha\rangle + |-\alpha\rangle)(|\alpha\rangle + |-\alpha\rangle)/2$. After performing the two-cavity CZ gate, the two-cavity state evolves into an entangled state $|\psi_1\rangle = (|\alpha\rangle|\alpha\rangle + |\alpha\rangle|-\alpha\rangle + |-\alpha\rangle|\alpha\rangle - |-\alpha\rangle|-\alpha\rangle)/2$ with a slight deformation due to Kerr effect. Figure S4 is the measured joint Wigner function of the entangled two-cavity state $|\psi_1\rangle$ in the Re-Re and Im-Im planes, which are consistent with our simulation results.

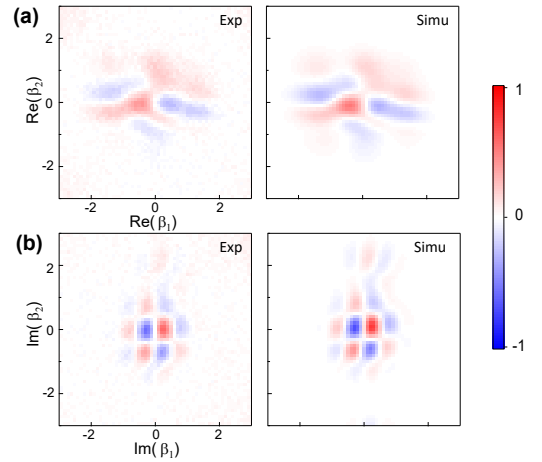


FIG. S4: Experimentally measured and simulated joint Wigner functions in the Re-Re plane (a) and Im-Im plane (b) for the entangled cavity states $|\psi_1\rangle$.

VII. TWO-CAVITY SNAP GATES

The geometric manipulation method can also be used to deterministically create high-fidelity single-photon Bell states $|\Phi_{\pm}\rangle = (|01\rangle_F \pm |10\rangle_F)/\sqrt{2}$, an extension of the previously reported SNAP operation for universal control of one cavity [20, 24] to two cavities. When combined with the single-cavity SNAP gates, our method can be used to realize arbitrary universal multi-cavity control. The experimental sequence is shown in Fig. S5(a), where a conditional 2π rotation on qubit Q_3 is sandwiched in between two pairs of phase-space displacements of the cavities. The four displacement amplitudes, $\alpha_1 = \mp 0.8082$, $\alpha_2 = -0.8082$, $\alpha_3 = \pm 0.4103$, and $\alpha_4 = 0.4103$, are calculated from numerical simulation and further optimized in experiment in order to achieve higher state fidelities. With help of the two ancillary qubits, joint Wigner tomography of the two cavities is performed and two slice cuts of the measured two-mode Wigner function are shown in Figs. S5(b-c). The density matrices of $|\Phi_{+}\rangle$ and

TABLE S4: Infidelities of the geometric gates. Error budgets for the single-cavity phase gate, two-cavity CZ gate with coherent encoding, and two-cavity CZ gate with binomial encoding. The conditional pulse selectivity error, the numerical optimization imperfection, and the self- and cross-Kerr induced error are considered as the control pulse imperfections.

Error sources	Single-cavity phase gate	Two-cavity CZ gate with coherent encoding	Two-cavity CZ gate with binomial encoding
Encoding/decoding error	0.03	0.05	0.08
Relaxation and dephasing	0.01	0.02	0.04
Conditional pulse selectivity error	<0.01	0.06	0.03
Numerical optimization imperfection	-	-	0.01
Self- and cross-Kerr induced error	<0.01	0.03	<0.01
Total	0.04	0.16	0.16

$|\Phi_{-}\rangle$, reconstructed by mapping the state of the two cavities to qubits Q_1 and Q_2 and then jointly measuring the state of these qubits, are displayed in Figs. S5(d), with state fidelities of 0.933 and 0.923, respectively. Single-cavity Wigner functions on storage cavities S_1 and S_2 have also been performed and are shown in Fig. S5(e-f). The measured single-cavity

Wigner functions indicate mixed states of Fock states $|0\rangle$ and $|1\rangle$ as expected. Therefore, these results manifest that the generated two-cavity states are no longer separable and the individual cavity measurement destroys the coherence between them.

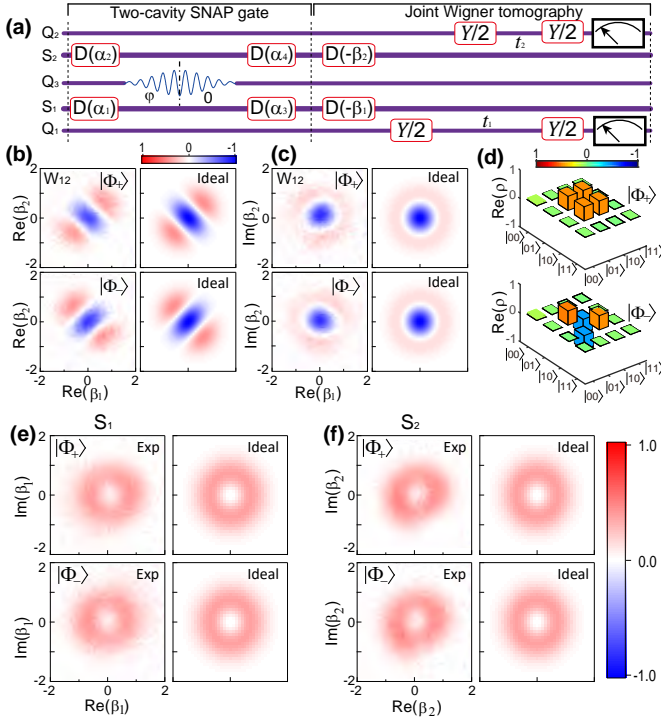


FIG. S5: Two-cavity SNAP gate to create single-photon Bell states $|\Phi_{\pm}\rangle = (|01\rangle_F \pm |10\rangle_F)/\sqrt{2}$. (a) Experimental sequence, which consists of a conditional 2π rotation on the qubit Q_3 and four displacements of the cavity states, followed by joint Wigner tomography measurements. (b) and (c) The measured joint Wigner function W_{12} of the Bell states $|\Phi_{+}\rangle$ and $|\Phi_{-}\rangle$ on the Re-Re and Im-Re planes, respectively. (d) Real parts of the density matrices of the states $|\Phi_{+}\rangle$ and $|\Phi_{-}\rangle$ measured with the decoding and state tomography. Solid black outlines are for the ideal density matrices. Measured imaginary parts for both states are smaller than 0.03 and not shown. The fidelities for $|\Phi_{\pm}\rangle$ are 0.933 and 0.923, respectively. (e) and (f) Single-cavity Wigner functions of the entangled states $|\Phi_{\pm}\rangle$, measured from the storage cavities S_1 and S_2 , respectively.

VIII. GATE ERROR ANALYSIS

In this section, we estimate the main error sources and their contributions to the loss of fidelity for the single-cavity phase gate, two-cavity CZ gate with coherent encoding, and two-cavity CZ gate with binomial encoding. The results are summarized in Table S4.

1. The encoding/decoding error can be estimated by the measured process fidelity F_{ED} with the encoding and decoding processes only. The encoding/decoding errors mainly come from the decoherence of the ancillary qubit, imperfection of the GRAPE optimization, and inaccuracy of the Hamiltonian parameter calibration.

2. The relaxation and dephasing errors come from the ancillary qubit decoherence during the geometric gates with a gate time T_{gate} . The ancillary qubit is in the excited state on average for half of the gate time during the selective pulse. Thus the average gate error induced by relaxation and dephasing can be estimated by $T_{gate}/2T_1$.

3. The selectivity error of the conditional qubit rotation, the numerical optimization imperfection, and the self- and cross-Kerr effects induced errors are considered as the control pulse imperfections and can be roughly estimated by the master equation simulation with only ideal operations. For the logical qubits with both coherent encoding and binomial encoding, the non-negligible self- and cross-Kerr terms in Hamiltonian Eq. S1 will result in deterministic and small deformation and rotation of the cavity states. In order to achieve high fidelity, we have partly compensated these deterministic effects by including them in the decoding pulses with numerical optimization.

The total estimated infidelities are consistent with the experimentally measured gate process fidelities F_{Gate_ED} , which include the encoding and decoding processes.

- [1] H. Paik, D. I. Schuster, L. S. Bishop, G. Kirchmair, G. Catelani, A. P. Sears, B. R. Johnson, M. J. Reagor, L. Frunzio, L. I. Glazman, S. M. Girvin, M. H. Devoret, and R. J. Schoelkopf, "Observation of high coherence in josephson junction qubits measured in a three-dimensional circuit qed architecture," *Phys. Rev. Lett.* **107**, 240501 (2011).
- [2] B. Vlastakis, G. Kirchmair, Z. Leghtas, S. E. Nigg, L. Frunzio, S. M. Girvin, M. Mirrahimi, M. H. Devoret, and R. J. Schoelkopf, "Deterministically encoding quantum information using 100-photon Schrödinger cat states," *Science* **342**, 607 (2013).
- [3] K. Liu, Y. Xu, W. Wang, S.-B. Zheng, T. Roy, S. Kundu, M. Chand, A. Ranadive, R. Vijay, Y. Song, *et al.*, "A twofold quantum delayed-choice experiment in a superconducting circuit," *Sci. Adv.* **3**, e1603159 (2017).
- [4] W. Wang, L. Hu, Y. Xu, K. Liu, Y. Ma, S.-B. Zheng, R. Vijay, Y. P. Song, L.-M. Duan, and L. Sun, "Converting quasiclassical states into arbitrary fock state superpositions in a superconducting circuit," *Phys. Rev. Lett.* **118**, 223604 (2017).
- [5] L. Hu, Y. Ma, W. Cai, X. Mu, Y. Xu, W. Wang, Y. Wu, H. Wang, Y. Song, C. Zou, S. M. Girvin, L.-M. Duan, and L. Sun, "Quantum error correction and universal gate set on a binomial bosonic logical qubit," *Nat. Phys.* **15**, 503 (2019).
- [6] Y. Xu, W. Cai, Y. Ma, X. Mu, L. Hu, T. Chen, H. Wang, Y. P. Song, Z.-Y. Xue, Z.-q. Yin, and L. Sun, "Single-loop realization of arbitrary nonadiabatic holonomic single-qubit quantum gates in a superconducting circuit," *Phys. Rev. Lett.* **121**, 110501 (2018).
- [7] M. Reagor, H. Paik, G. Catelani, L. Sun, C. Axline, E. Holland, I. M. Pop, N. A. Masluk, T. Brecht, L. Frunzio, M. H. Devoret, L. Glazman, and R. J. Schoelkopf, "Reaching 10 ms single photon lifetimes for superconducting aluminum cavities," *Applied Physics Letters* **102**, 192604 (2013).
- [8] M. Reagor, W. Pfaff, C. Axline, R. W. Heeres, N. Ofek, K. Sliwa, E. Holland, C. Wang, J. Blumoff, K. Chou, M. J. Hatridge, L. Frunzio, M. H. Devoret, L. Jiang, and R. J. Schoelkopf, "Quantum memory with millisecond coherence in circuit qed," *Phys. Rev. B* **94**, 014506 (2016).
- [9] C. Wang, Y. Y. Gao, P. Reinhold, R. W. Heeres, N. Ofek, K. Chou, C. Axline, M. Reagor, J. Blumoff, K. Sliwa, *et al.*, "A schrödinger cat living in two boxes," *Science* **352**, 1087 (2016).
- [10] Y. Y. Gao, B. J. Lester, K. S. Chou, L. Frunzio, M. H. Devoret, L. Jiang, S. M. Girvin, and R. J. Schoelkopf, "Entanglement of bosonic modes through an engineered exchange interaction," *Nature* **566**, 509 (2019).
- [11] N. Khaneja, T. Reiss, C. Kehlet, T. Schulte-Herbrüggen, and S. J. Glaser, "Optimal control of coupled spin dynamics: design of NMR pulse sequences by gradient ascent algorithms," *J. Magn. Reson.* **172**, 296 (2005).
- [12] P. de Fouquieres, S. Schirmer, S. Glaser, and I. Kuprov, "Second order gradient ascent pulse engineering," *J. Magn. Reson.* **212**, 412 (2011).
- [13] F. Motzoi, J. M. Gambetta, P. Rebentrost, and F. K. Wilhelm, "Simple Pulses for Elimination of Leakage in Weakly Nonlinear Qubits," *Phys. Rev. Lett.* **103**, 110501 (2009).
- [14] J. M. Gambetta, F. Motzoi, S. T. Merkel, and F. K. Wilhelm, "Analytic control methods for high-fidelity unitary operations in a weakly nonlinear oscillator," *Phys. Rev. A* **83**, 012308 (2011).
- [15] E. Knill, D. Leibfried, R. Reichle, J. Britton, R. B. Blakestad, J. D. Jost, C. Langer, R. Ozeri, S. Seidelin, and D. J. Wineland, "Randomized benchmarking of quantum gates," *Phys. Rev. A* **77**, 012307 (2008).
- [16] J. M. Chow, J. M. Gambetta, L. Tornberg, J. Koch, L. S. Bishop, A. A. Houck, B. R. Johnson, L. Frunzio, S. M. Girvin, and R. J. Schoelkopf, "Randomized benchmarking and process tomography for gate errors in a solid-state qubit," *Phys. Rev. Lett.* **102**, 090502 (2009).
- [17] E. Magesan, J. M. Gambetta, B. R. Johnson, C. A. Ryan, J. M. Chow, S. T. Merkel, M. P. da Silva, G. A. Keefe, M. B. Rothwell, T. A. Ohki, M. B. Ketchen, and M. Steffen, "Efficient measurement of quantum gate error by interleaved randomized benchmarking," *Phys. Rev. Lett.* **109**, 080505 (2012).
- [18] E. Magesan, J. M. Gambetta, and J. Emerson, "Scalable and robust randomized benchmarking of quantum processes," *Phys. Rev. Lett.* **106**, 180504 (2011).
- [19] R. Barends, J. Kelly, A. Megrant, A. Veitia, D. Sank, E. Jeffrey, T. C. White, J. Mutus, A. G. Fowler, B. Campbell, Y. Chen, Z. Chen, B. Chiaro, A. Dunsworth, C. Neill, P. O'Malley, P. Roushan, A. Vainsencher, J. Wenner, A. N. Korotkov, A. N. Cleland, and J. M. Martinis, "Superconducting quantum circuits at the surface code threshold for fault tolerance," *Nature* **508**, 500 (2014).
- [20] R. W. Heeres, B. Vlastakis, E. Holland, S. Krastanov, V. V. Albert, L. Frunzio, L. Jiang, and R. J. Schoelkopf, "Cavity state manipulation using photon-number selective phase gates," *Phys. Rev. Lett.* **115**, 137002 (2015).
- [21] M. A. Nielsen and I. L. Chuang, *Quantum Computation and Quantum Information* (Cambridge Univ. Press, 2000).
- [22] D. F. V. James, P. G. Kwiat, W. J. Munro, and A. G. White, "Measurement of qubits," *Phys. Rev. A* **64**, 052312 (2001).
- [23] J. M. Chow, J. M. Gambetta, A. D. Córcoles, S. T. Merkel, J. A. Smolin, C. Rigetti, S. Poletto, G. A. Keefe, M. B. Rothwell, J. R. Rozen, M. B. Ketchen, and M. Steffen, "Universal quantum gate set approaching fault-tolerant thresholds with superconducting qubits," *Phys. Rev. Lett.* **109**, 060501 (2012).
- [24] S. Krastanov, V. V. Albert, C. Shen, C.-L. Zou, R. W. Heeres, B. Vlastakis, R. J. Schoelkopf, and L. Jiang, "Universal control of an oscillator with dispersive coupling to a qubit," *Phys. Rev. A* **92**, 040303 (2015).